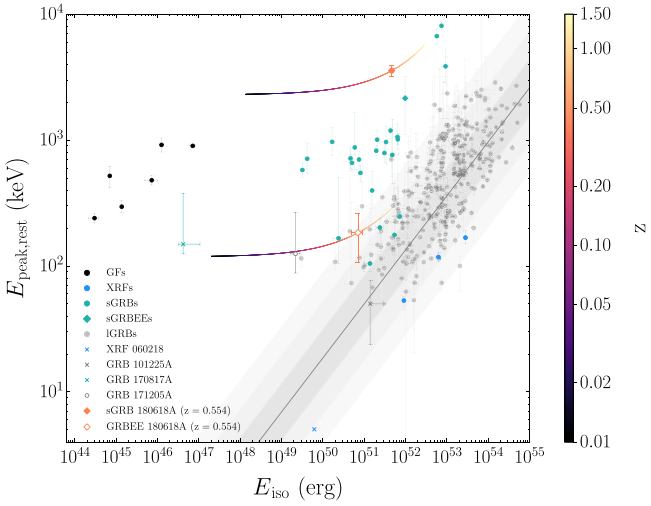

Figure 10. Rest-frame peak energy ($E_{\rm peak}$) and isotropic-equivalent energy ($E_{\rm iso}$) of short GRB 180618A and its extended gamma-ray emission at redshift $z = 0.554$. The GRB 180618A high-energy parameters are also displayed for the redshift range $z = 0.01$–1.5. For reference, we include those GRBs with known redshifts classified as giant flares from magnetars (GFs; Zhang et al. 2020), short GRBs (sGRBs; D'Avanzo et al. 2014; Calderone et al. 2015; Tsvetkova et al. 2017, 2021), short GRBs with extended gamma-ray emission (sGRBEEs; D'Avanzo et al. 2014), long GRBs (lGRBs; Tsvetkova et al. 2017, 2021), and X-ray flashes (XRFs; Tsvetkova et al. 2021). For the population of long GRBs, we represent the best-fitting line from Tsvetkova et al. 2021, and the corresponding 1σ, 2σ, 3σ confidence levels. We also add the GRB counterpart of gravitational wave event GW170817 (Zhang et al. 2018), and three GRBs with early afterglows interpreted as blackbody emission from either a thermalized jet or cocoon: XRF 060218 (Campana et al. 2006; Thöne et al. 2011), GRB 101225A (Thöne et al. 2011), and GRB 171205A (D'Elia et al. 2018; Izzo et al. 2019).

and not compatible with the long GRB population. Overall, the gamma-ray properties and the GRB–host galaxy offset confirm the merger nature of GRB 180618A (see, e.g., Zhang et al. 2009; Rastinejad et al. 2022).

4. Interpretation and Modeling

The overall temporal and spectral evolution of the optical emission ($\Delta\alpha_{\rm opt} = 4.2$, $\Delta\beta_{\rm opt} = 3.3$; see Figure 2) are hard to explain just in terms of the flaring activity (i.e., $\Delta t/t > 1$; Zhang et al. 2006) or the external shock from the decelerating relativistic ejecta (i.e., the afterglow; Piran 1999; Kobayashi 2000). The observed decay rates of the emission do not agree with $\alpha \approx 1$ expected from forward shock emission with a typical electron index of the synchrotron energy spectrum, and the break cannot be reconciled with the passage of the synchrotron cooling frequency (Sari et al. 1998). We also discard the fast-fading emission from the reverse shock (Kobayashi 2000), which typically decays with index $\alpha \approx 2$ —still slower than in GRB 180618A. A reverse-shock scenario further disagrees with the rapid spectral evolution of the optical emission at the time of the light-curve break, and the nondetection of high values of polarization during the broad optical peak (Mundell et al. 2013). Finally, we rule out that the optical break is an effect of the relativistic collimation of the outflow given that there is no simultaneous steepening of the emission across the spectrum at that time (Sari 1999; Racusin et al. 2009).

We suggest that the spectral evolution and rapid decline in the optical emission of GRB 180618A is produced by thermal emission (e.g., Thöne et al. 2011; Izzo et al. 2019). In

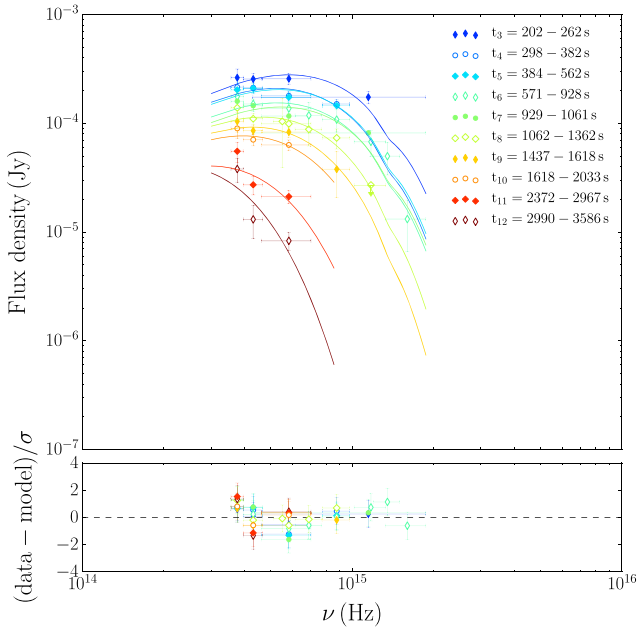

Figure 11. GRB 180618A best-fitting blackbody models to joint RINGO3/UVOT data at the observer rest frame. Note that the model accounts for Galactic dust extinction but does not include the host galaxy dust contribution.

Section 4.1, we model the ultraviolet to optical emission with a blackbody model. Following, we discuss if the radioactive decay of the *r*-processed ejecta from the merger or a thermalized jet are credible interpretations to explain the origin of the bright thermal emission. In Section 4.2, we find evidence of a magnetar wind nebula powering thermal optical emission for 15–60 minutes after GRB 180618A—suggesting that emission before that time is due to the jet afterglow. In Section 4.3, we detail the properties of the magnetar powering the distinct nonthermal emission components, from gamma rays to optical wavelengths. In Section 4.4, we model the overall (X-ray to optical) spectra with physical synchrotron models. This analysis proves Section 4.2 findings; the emission until 3–15 minutes post-burst is due to the jet afterglow and that corresponding to 15–60 minutes post-burst requires an extra spectral component (i.e., thermal emission). In Section 4.5, we test closure relations, and we suggest that the jet geometry and observer viewing angle are key to detecting the thermal emission.

4.1. Thermal Emission

In Xspec, we modeled the co-temporal UVOT and RINGO3 data with a blackbody profile that includes Milky Way dust absorption (see Figure 11). At the observer rest frame, the best-fitting effective temperatures and luminosities from the blackbody models evolve from $T_{\rm eff} = (1.1 \pm 0.1) \times 10^4$ K and $L_{\rm th}/D_{\rm L}^2 = (4.3 \pm 0.5) \times 10^{44}$ erg s^{-1} Gpc^{-2} at $t = 202$–262 s post-burst to $T_{\rm eff} = (3.8 \pm 0.6) \times 10^3$ K and $L_{\rm th}/D_{\rm L}^2 = (1.8 \pm 0.6) \times 10^{43}$ erg s^{-1} Gpc^{-2} at $t = 2990$–3586 s post-burst (see results in Table 3), where $D_{\rm L}$ is the luminosity distance. Note that the data are well fitted by the model without the need of the host galaxy dust extinction component, which is consistent with the large offset of short GRB 180618A with the host galaxy core (i.e., ≈10 kpc).

Faint thermal emission at optical and infrared wavelengths has been detected emerging hours to days after short GRBs

Table 3
GRB 180618A Effective Temperatures ($T_{\rm eff}$) and Luminosities ($L_{\rm th}/D_{\rm L}^2$) Derived from the Best-fitting Blackbody Models to Joint RINGO3/UVOT Data

$t_{\rm mid}$-T_0 (s)	$t_{\rm err}$ (s)	$T_{\rm eff}$ (10^3 K)	$T_{\rm eff,err}$ (10^3 K)	$L_{\rm th}/D_{\rm L}^2$ (10^{43} erg s^{-1} Gpc^{-2})	$L_{\rm th,err}/D_{\rm L}^2$ (10^{43} erg s^{-1} Gpc^{-2})
231	30	10.9	1.0	42.6	5.3
340	42	9.8	0.7	27.9	2.2
473	89	10.0	0.5	27.9	0.7
749	179	9.8	0.6	20.7	1.7
995	67	10.2	0.6	19.8	1.0
1212	150	8.6	0.9	13.0	1.5
1528	90	7.8	1.1	9.4	1.2
1825	208	7.2	1.2	7.1	0.9
2670	298	5.3	0.9	2.6	0.3
3288	298	3.8	0.6	1.8	0.6

Note. $t_{\rm mid}$ is the mean observing time, T_0 is the BAT trigger time, $t_{\rm err}$ is half the length of the observing time window, and $D_{\rm L}$ is the luminosity distance. Note that the model does not account for host galaxy extinction.

(Tanvir et al. 2013; Abbott et al. 2017a)—when the relatively brighter afterglow has subsided. This emission has been attributed to a kilonova (Metzger et al. 2010; Roberts et al. 2011)—a type of emission powered by the radioactive decay of the heavy elements formed after the dynamically ejected and wind-driven neutron-rich material of the merger expands from nuclear densities and neutrons are captured via the *r* process. Predictions are that an ultraviolet kilonova precursor could also be detected from the decay of free neutrons in the fast material (Metzger et al. 2015). However, the short timescales of the GRB 180618A optical emission do not support *r*-process models, for which we also expect lower peak luminosities ($L_{\rm th} = 10^{40}$–10^{42} erg s^{-1}; Metzger et al. 2010, 2015) than those estimated in GRB 180618A, i.e., $L_{\rm th}(z = 0.554) \approx 2 \times 10^{45}$ erg s^{-1}.

We also discard thermal emission powered by the GRB jet. The measured luminosities and effective temperatures do not follow the scalings expected from thermal emission of the relativistic and nonrelativistic material of the jet cocoon (Nakar & Piran 2017; De Colle et al. 2018). Similarly, maximizing the signal from the jet cocoon at $z = 0.554$ corresponds to a very energetic long GRB and large energy stored in the jet cocoon, on the order of $E_{\rm c} \approx 10^{52}$ erg (Nakar & Piran 2017). This would be expected to produce at most a ≈22 mag near-ultraviolet and ≈23.6 mag optical thermal rebrightening. These values are not consistent with the observed peak luminosities of the thermal emission (e.g., ≈18 mag in the UVOT *uvw1* band, and ≈18.7 mag in the RINGO3 *BV* band), and they are far below the limiting magnitude of our UVOT and RINGO3 observations. Furthermore, successful jets in energetic engines like GRB 180618A are expected to have an early breakout from the stellar envelope, which cuts thermalization and leads to most of the jet energy leaving the ejecta (Ramirez-Ruiz et al. 2002; Duffell et al. 2018; Izzo et al. 2019).

4.2. Thermal Emission from a Relativistically Expanding Magnetar Wind Nebula

Here, we explore the possibility that the observed thermal emission from GRB 180618A could be explained by a magnetar wind nebula (Yu et al. 2013; Metzger & Piro 2014; Gao et al. 2015; Wollaeger et al. 2019) and the implications of such a model for this system.

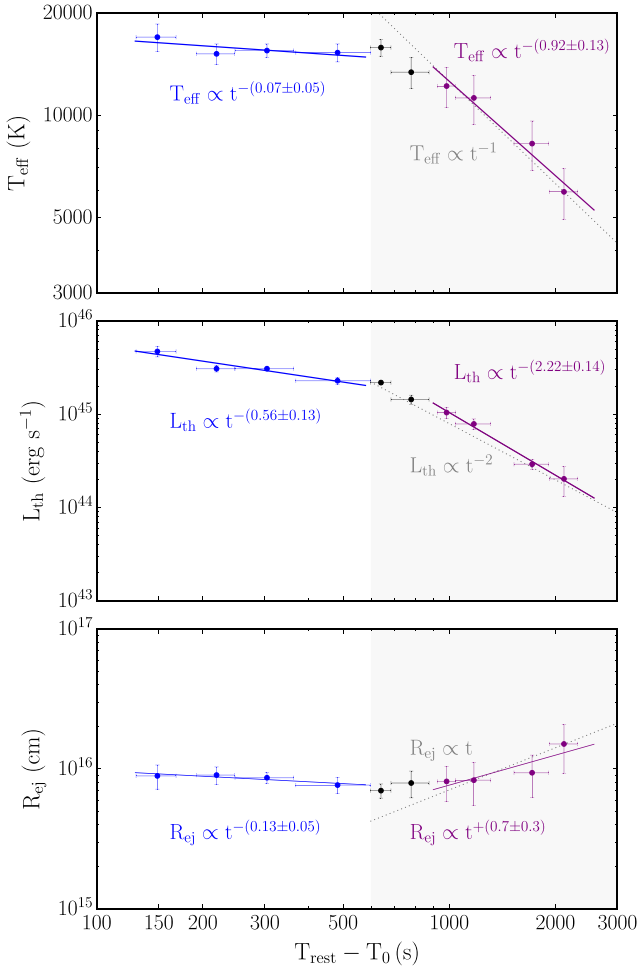

Figure 12. Temporal evolution of the effective temperatures ($T_{\rm eff}$), luminosities ($L_{\rm th}$), and photospheric radii ($R_{\rm ej}$) of the best-fitting blackbody models at the host galaxy rest frame (i.e., $z = 0.554$). The shaded gray area corresponds to the thermal contribution from the magnetar wind nebula, and the dotted gray line is the expected evolution of the temperature, luminosity, and radius for an optically thin regime.

In a magnetar wind nebula, the expanding ejecta shell is continually being heated from behind by the magnetar winds—a scenario that differs from fireball models with energy injection at a single point in time (e.g., Mészáros & Rees 1997; Nakar & Piran 2017). As such, the thermal luminosity is expected to track the spin-down luminosity of the magnetar as $L_{\rm th} \propto L_{\rm sd} \propto t^{-2}$ (Yu et al. 2013; Metzger & Piro 2014). Assuming that the ejecta radially expands as $R_{\rm ej} \propto t$, the effective temperatures are expected to follow $T_{\rm eff} = [L_{\rm th}/(4\pi\sigma_{\rm B} R_{\rm ej}^2)]^{1/4} \propto L_{\rm th}^{1/4} t^{-1/2} \propto t^{-1}$, where $\sigma_{\rm B}$ is the Stefan–Boltzmann constant.

In Figure 12, we model the temporal evolution of the best-fitting effective temperatures, luminosities, and photospheric radii ($R_{\rm ej}$) with power laws. For data ≈1400 s post-burst, we find that the observed scalings $L_{\rm th} \propto t^{-(2.22\pm0.14)}$, $T_{\rm eff} \propto t^{-(0.92\pm0.13)}$, and $R_{\rm ej} \propto t^{+(0.7\pm0.3)}$ are compatible with those expected in a magnetar nebula (Metzger & Piro 2014). The peak luminosity $L_{\rm th}(z = 0.554) \approx 2 \times 10^{45}$ erg s^{-1} of GRB 180618A is also within the expected values (Yu et al. 2013; Metzger & Piro 2014). Note that data 900–1400 s post-burst are

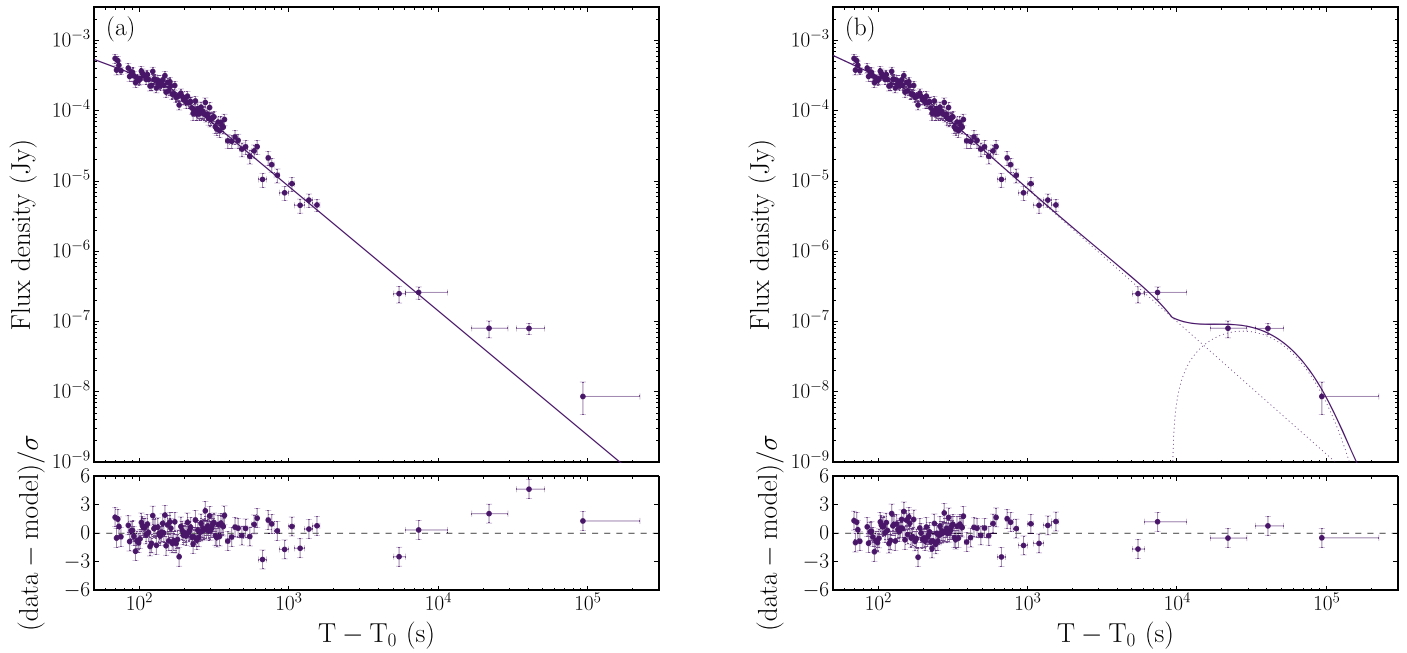

Figure 13. Best-fitting models of the XRT X-ray light curve of GRB 180618A. (a) Broken power-law model. The best-fitting parameters are an initial decay rate of $\alpha_{X,1} = 0.79 \pm 0.12$, steeping to $\alpha_{X,2} = 1.77 \pm 0.04$ at $t_{break} = 162 \pm 11$ s (χ^2/dof = 131/102). (b) Broken power-law model plus a pulse function, with $\alpha_{X,1} = 0.99 \pm 0.07$, $\alpha_{X,2} = 1.89 \pm 0.06$, $t_{break} = 206 \pm 14$ s (χ^2/dof = 104/99). The bottom panels are the residuals of the best-fitting model.

still in agreement with the model, and that the deviation we detect is likely due to the contribution from the external shock, which dominates the emission before 900 s post-burst (see Section 4.4).

A newborn millisecond magnetar from a binary neutron star merger is expected to be close to the centrifugal breakup limit (Giacomazzo & Perna 2013; Fryer et al. 2015), with an initial spin period of $P_i \approx 1$ ms. Consequently, ejecta below a critical mass $M_{ej} \approx 10^{-2} M_\odot P_i^{-2}$ can be accelerated to transrelativistic speeds ($\Gamma \geqslant 1$) by the magnetar wind (Gao et al. 2013; Yu et al. 2013), where $\Gamma = (1 - \beta^2)^{-1/2}$ is the Lorentz factor, and $\beta = v/c$ is the ratio of the velocity between the inertial reference frames and the speed of light in vacuum. From the photospheric radius of the best-fitting blackbody model at the engine rest frame, $R'_{ej} = ct' \approx ct_{obs}(1+z)^{-1}(1-\beta)^{-1} \approx 2\Gamma^2 ct_{obs}(1+z)^{-1}$, we find that the ejecta in the GRB 180618A system is expanding at mildly relativistic speeds, i.e., $\Gamma(z = 0.554) \approx 9$.

For such low ejecta masses giving rise to high Lorentz factors, the ejecta can become optically thin before the diffusion time (Yu et al. 2013), i.e., when the optical depth $\tau' = (3M_{ej}\kappa)/(4\pi R'^2) \approx 1$, where κ is the opacity and M_{ej} is the isotropic-equivalent mass of the ejecta. The optical depth can be significantly raised (for a total mass in the shell) given electron–positron pair creation in the region behind the ejecta shell (Metzger & Piro 2014). We estimate the maximum pair multiplicity by assuming that a fraction ≈0.1 of the magnetar rotational energy $E_{rot} \approx 10^{52}$ erg is converted through a pair cascade process into electron–positron pairs in the nebula (Metzger & Piro 2014), such that $\kappa_\pm \approx (0.1 E_{rot}/m_e c^2)(m_p/M_{ej}) \approx 10^3 (M_{ej}/10^{-3} M_\odot)^{-1}$. That is, pairs contribute $\approx 10^3$ times to the opacity for their mass than an electron–ion outflow, with a typical electron-scattering opacity of $\kappa \approx 0.2$ cm^2 g^{-1} (Yu et al. 2013; Metzger et al. 2015). Given an electron–positron annihilation rate slower than the outflow expansion speed at late times (Metzger & Piro 2014), the pair opacity will still dominate the total opacity by the time of observations. Therefore, assuming an optically thin regime ($\tau' \lesssim 1$) when we start to notice the thermal emission ($t_{obs} \lesssim 10^3$ s) and opacity $\kappa \approx (0.2 \text{ cm}^2 \text{ g}^{-1})\,\kappa_\pm$, we estimate ejecta masses $M_{ej} \lesssim 10^{-4} M_\odot (\kappa_\pm/10^3)^{-1}$ at the polar regions of the system. This is consistent with the mass loss expected from merger remnants (e.g., Oechslin & Janka 2006; Lee & Ramirez-Ruiz 2007).

4.3. Nonthermal Emission from a Magnetar Wind Nebula

We used the GRB 180618A pipeline-processed products of the Swift XRT (Burrows et al. 2005; Evans et al. 2009), and we modeled the 0.3−10 keV light curve with a broken power-law function (see Figure 13(a)). We find a significant emission excess of 4.6σ at $t \approx 4 \times 10^4$ s post-burst, which we modeled with a pulse function (Piranomonte et al. 2008), i.e., $F = F_0 (t - t_0) e^{-(t-t_0)/\tau_\sigma}$. The best-fitting parameters of this model are an initial emission decay rate of $\alpha_{X,1} = 0.99 \pm 0.07$ and a break at $t_{break} = 206 \pm 14$ s post-burst followed by a steeper decay with $\alpha_{X,2} = 1.89 \pm 0.06$ (see Figure 13(b)). For the late-time rebrightening, we find $t_0 = (9.3 \pm 3.8) \times 10^3$ s and $\tau_\sigma = (1.8 \pm 0.3) \times 10^4$ s.

If the magnetar winds are powerful enough and the ejecta mass is low, the nebula can be fully ionized at late times and X-ray emission will be able to leak out the nebula (Metzger & Piro 2014; Gao et al. 2015). This is consistent with the X-ray late-time rebrightening of GRB 180618A and implies that we are directly detecting the magnetar spin-down luminosity. This emission is expected to follow $L_{sd} = L_0 (1 + t/t_{sd})^{-2}$ with typical values $L_0 = 1.7 \times 10^{50} B_{15}^2 P_{i,-3}^{-4}$ erg s^{-1} and $t_{sd} = 307 B_{15}^{-2} P_{i,-3}^2$ s (e.g., Metzger 2019), which correspond to a cooled neutron star of 12 km fiducial radius (Beznogov et al. 2020), magnetic field $B_{15} \approx 10^{15}$ G, and initial spin $P_{i,-3} \approx 1$ ms (see, e.g., Rosswog et al. 2003).

At early times ($t \ll t_{sd}$), the luminosity of the magnetar from GRB 180618A is estimated to be $L_0 \approx L_{iso} f_b/\eta$, where $f_b \approx \theta_{j,EE}^2/2$ is the beaming factor, η is the radiative efficiency,

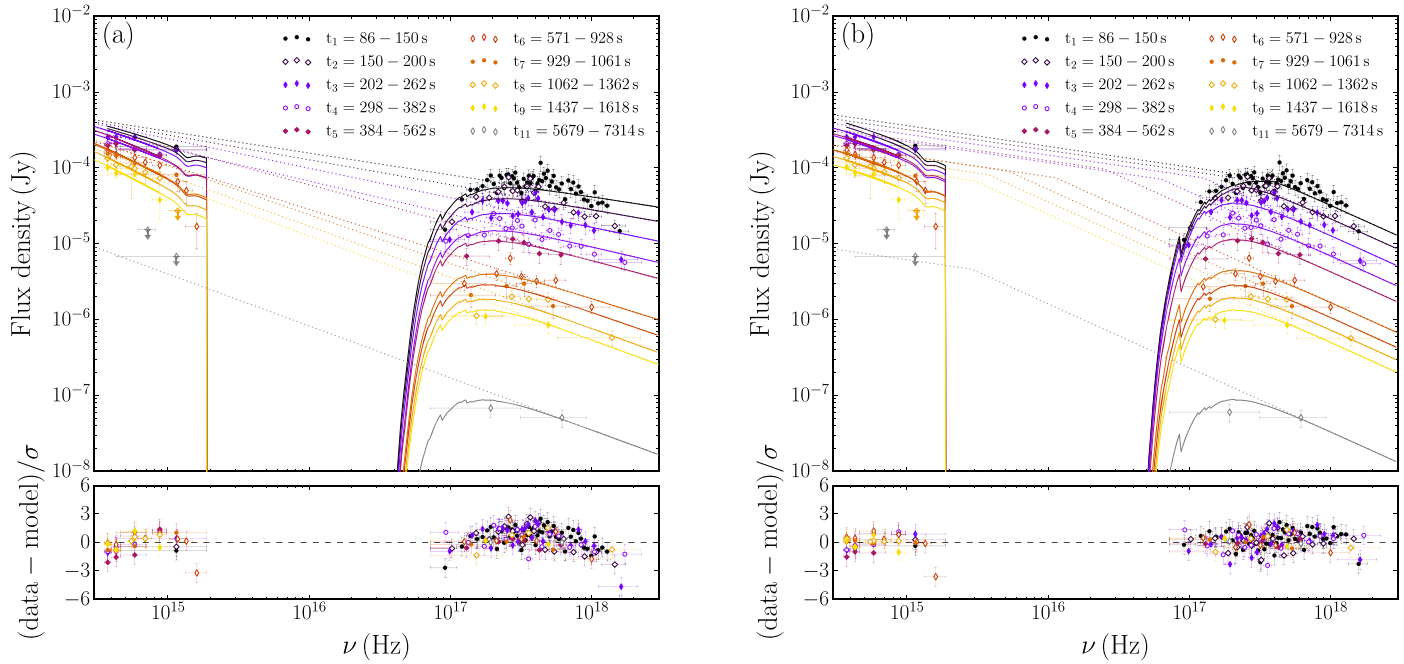

Figure 14. Spectral energy distributions of the co-temporal X-ray, optical, and ultraviolet observations of GRB 180618A. The XRT, UVOT, and RINGO3 data are modeled with the following synchrotron models. (a) Power laws (χ^2/dof = 292/159). (b) Broken power laws with a joint optical and X-ray spectral indexes (χ^2/dof = 170/158). The best-fitting spectral indexes are $\beta_{\rm opt} = 0.27 \pm 0.02$ and $\beta_{\rm X} = 0.84 \pm 0.05$. Note that we have fixed the break of the t_{11} epoch (gray color) to the t_{10} epoch value given the optical upper limits. In dotted lines, we show the best-fitting synchrotron model and in solid lines the model that includes the dust and hydrogen absorption from the Milky Way and host galaxy for a redshift $z = 0.554$. Detections have 1σ error bars, and nondetections are presented as 3σ upper limits.

and $\theta_{\rm j,EE}$ is the jet opening angle. For a redshift $z = 0.554$ and assuming a large opening angle for the magnetar wind (i.e., $f_{\rm b}/\eta \approx 1$; Bucciantini et al. 2012), the characteristic luminosity is $L_0(z = 0.554) \approx 2 \times 10^{49}$ erg s^{-1}. Furthermore, for a rebrightening of $L_{\rm X}(z = 0.554) \approx 4 \times 10^{44}$ erg s^{-1} at $t \approx 5 \times 10^4\,(1+z)^{-1}$ s post-burst, the characteristic spin-down time of the magnetar needs to be $t_{\rm sd} \approx 200(1+z)^{-1}$ s. Note that this is consistent with the early optical plateau of the UVOT *white* band that we detect with a decay rate of $\alpha_{\rm opt,white} = 0.12 \pm 0.08$ at $t \lesssim 200$ s post-burst (see also Rowlinson et al. 2013; Knust et al. 2017). Given all these constraints, we estimate the initial spin of the magnetar remnant of GRB 180618A to be $P_{\rm i} \approx 4$ ms, with a magnetic field of $B \approx 6 \times 10^{15}$ G.

In the magnetar scenario, a multiwavelength rebrightening could also be detectable hours to days post-burst given the deceleration of the mildly relativistic ejecta by the circumburst medium (Gao et al. 2013). At redshift $z = 0.554$, testing this prediction would have required sensitive late-time observations (e.g., Perley et al. 2009). That is, given typical values of the circumburst medium for a ≈10 kpc GRB–host galaxy offset ($n \lesssim 10^{-3}$ cm^{-3}; Fong et al. 2015), the best-case scenario for GRB 180618A corresponds to an emission excess with peak luminosity $\lesssim 10^{-9}$ Jy at X-ray bands, $\lesssim$25 mag at optical bands, and $\lesssim 100\,\mu$Jy at radio bands (Gao et al. 2013).

4.4. Nonthermal Emission from the Afterglow

The deceleration of the relativistic ejecta by the circumburst medium should also have left an early imprint on the overall emission. To reproduce the synchrotron spectrum of this external shock (Piran 1999), we modeled the joint optical and X-ray spectral energy distributions with absorbed power laws and broken power laws in Xspec (see Figures 14(a), (b)). Given the spectral slopes and the progression of the break to lower frequencies, we find that there must be at least one break frequency in between the bands and that it must be either the synchrotron or cooling frequency in an interstellar medium (Chevalier & Li 2000).

For the data after the X-ray light-curve break and the optical plateau, we tried two physical models for the GRB synchrotron spectrum: the fast and slow cooling of the electrons (e.g., Piran 1999). The best-fitting synchrotron models display trends in the residuals and suggest an additional spectral component at optical bands (see Figures 15(a), (b)). Therefore, having in mind the findings in Section 4.2, we introduced a blackbody profile in the model (see Figures 15(c), (d)). The best-fitting synchrotron plus blackbody model suggests a synchrotron spectrum with a rather hard electron index ($p = 1.6 \pm 0.1$ with spectral slopes $\beta_{\rm opt} = \beta_{\rm opt,PI} - 1 = 0.30 \pm 0.06$ and $\beta_{\rm X} = \beta_{\rm opt} + 0.5$), an interstellar medium profile, a slow-cooling regime, the cooling frequency in between the optical and X-ray bands, a blackbody profile contributing from ≈900 s post-burst, and low host galaxy dust extinction, i.e., $E(B-V)_{\rm HG} < 0.02$ —consistent with the GRB 180618A–host galaxy large offset. Additionally, we note that the constraint on polarization of $P_{\rm BV} < 6.1\%$ at early times supports the scenario of unpolarized forward shocks in short GRBs (see, e.g., Jordana-Mitjans et al. 2021 for long GRBs).

This physical model suggests that when the thermal emission subsides, we should detect the underlying afterglow again. Around 3300 s post-burst, the fast-fading afterglow emission should be $F_\nu \approx 7 \times 10^{-6}$ Jy, which we speculate that it is consistent with the subtle light-curve flattening of the RINGO3 *BV* band, with $F_\nu = (9 \pm 3) \times 10^{-6}$ Jy. Furthermore, the emission across the optical and X-ray bands is decaying faster than expected for spherical expansion (Racusin et al. 2009) and suggests a collimated relativistic outflow.

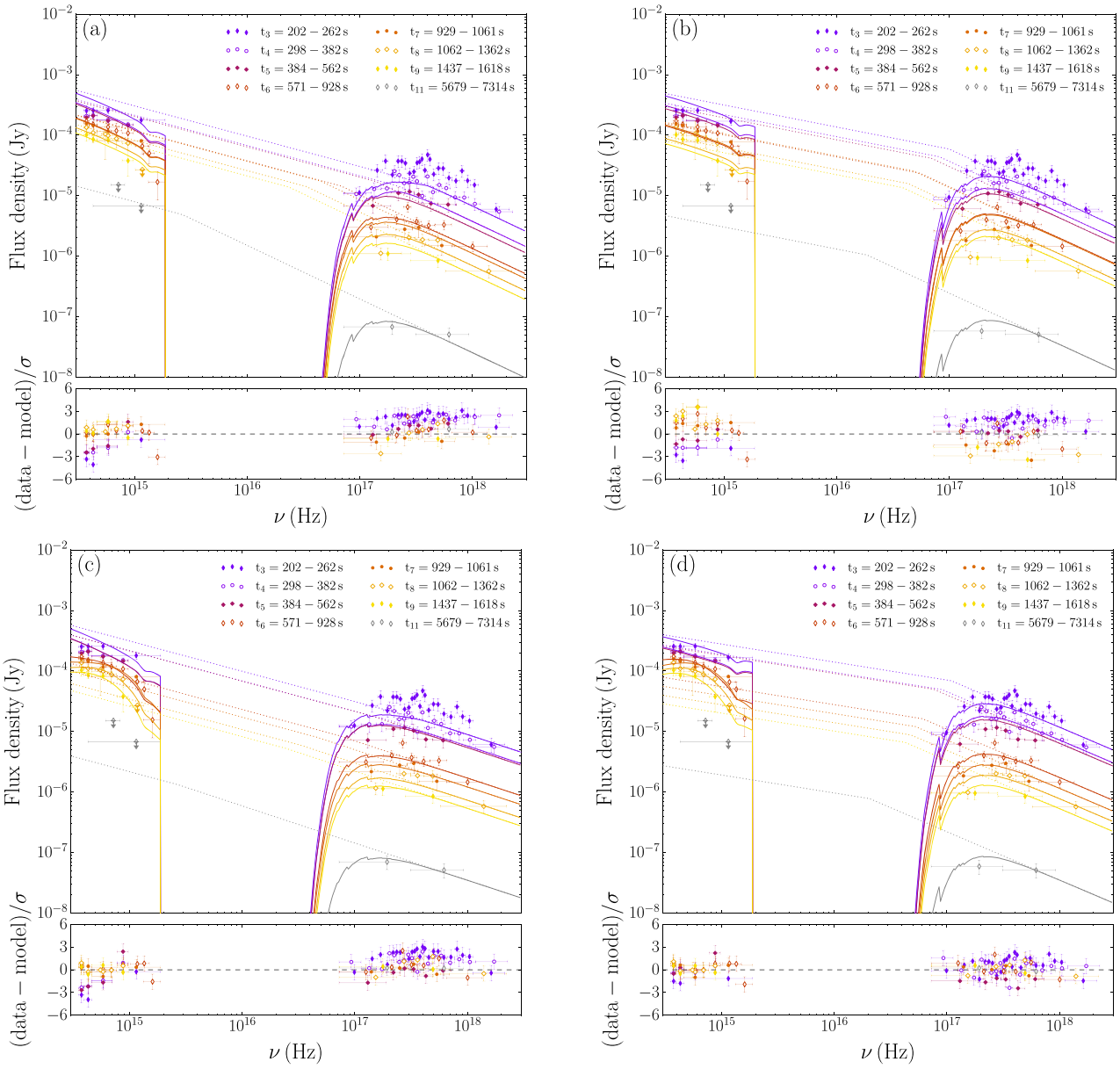

Figure 15. Spectral energy distributions of the co-temporal X-ray, optical, and ultraviolet observations of GRB 180618A. The data after the *white*-band UVOT plateau (i.e., $\gtrsim 200$ s post-burst) are modeled with the following physical models. (a) Fast cooling of the electrons ($\chi^2/\mathrm{dof} = 309/90$). That is, we fix the optical spectral index to $\beta_{\rm opt} = \beta_{\rm opt,PI} - 1 = 0.5$, and we let the synchrotron frequency evolve as $\nu_{\rm m} \propto t^{-1.5}$. (b) Slow cooling of the electrons ($\chi^2/\mathrm{dof} = 330/90$), i.e., we fix $\beta_{\rm X} = \beta_{\rm opt} + 0.5$ and the cooling frequency $\nu_{\rm c} \propto t^{-0.5}$. (c) Fast cooling and a blackbody profile ($\chi^2/\mathrm{dof} = 231/82$). (d) Slow cooling and a blackbody profile ($\chi^2/\mathrm{dof} = 106/82$). The best-fitting optical spectral index is $\beta_{\rm opt} = 0.30 \pm 0.08$ ($\beta_{\rm X} = \beta_{\rm opt} + 0.5$), which corresponds to an electron index $p = 1.6 \pm 0.1$. The dust contribution from the host galaxy is estimated to be $E(B-V)_{\rm HG} < 0.02$.

4.5. A Collimated Outflow

The temporal and spectral properties of the early X-ray emission of GRB 180618A satisfy closure relations for a jetted outflow with a hard electron index. That is, the first light-curve segment corresponds to the normal spherical decay rate of the afterglow (with average $\alpha_{\rm X} \approx 1.2$) and the second segment to the post-jet-break decay ($\alpha_{\rm X} \approx 2$; Racusin et al. 2009). For an interstellar medium profile, a slow-cooling regime, and with the X-ray band above the cooling frequency, a mean spectral index of $\beta_{\rm X} = 0.80 \pm 0.06$ implies an electron index of $p = 1.6 \pm 0.1$; see also the temporal evolution of $\beta_{\rm X}$ in Figure 2 (bottom panel). We find a temporal slope of $\alpha_{\rm X,1} = (3\beta_{\rm X} + 5)/8 = 0.93 \pm 0.02$ for the normal spherical decay of the afterglow and $\alpha_{\rm X,2} = (\beta_{\rm X} + 3)/2 = 1.90 \pm 0.03$ after the light-curve jet break, for an uniform jet scenario with lateral spreading (Zhang & Mészáros 2004; Racusin et al. 2009)—consistent with the observed decay rates of the X-ray light curve. Accounting for the early jet break at $t \approx 200$ s post-burst (Sari et al. 1999) and the fact that we are detecting the bright gamma-ray prompt emission (Yamazaki et al. 2002), we suggest that the observer faces the jet with a line of sight that likely runs near the jet edge. Overall, GRB 180618A suggests that the degree of collimation (Fong et al. 2015) and the observer viewing angle are key in detecting the short-lived optical thermal emission (and the late-time X-ray rebrightening) in short GRBs.